ARTICLE     OPEN

Check for updates

# Anthropogenic forcing and Pacific internal variability-determined decadal increase in summer precipitation over the Asian water tower

Yong Liu [1,2 ✉], Huijun Wang[3,4 ✉], Huopo Chen[3], Zhongshi Zhang[1,2], Hua Li[5] and Bo Liu[1,2]

The increased precipitation in the Asian water tower has prompted the abrupt lake expansion and increased runoff, significantly reshaping the water resource redistribution in the Inner Tibetan Plateau (ITP). However, the dynamic attribution behind this decadal increment remains unclear. Here, analysis of observations, large ensemble simulations, and pacemaker experiments indicates that this decadal increase was mainly attributed to the synergistic effects of the external forcing (anthropogenic greenhouse and aerosol emissions) and the Pacific internal variability, while the Atlantic and the Indian Ocean play a secondary role. Observations and simulations show that thermodynamic and dynamic effects work collaboratively to this increase. Remarkably, the upper-level dynamic convergence over the ITP would be enhanced through teleconnection and atmospheric dynamic feedback when involving the Pacific internal variability, resulting in more precipitation occurrence. Further analyses show that the enhanced stationary Rossby wave propagation over Eurasia and strengthened transient eddy activity over North Pacific could contribute to the anomalous cyclone over the ITP and weakened East Asian westerly jet, which built a pathway for the external forcing and Pacific internal variability collaboratively impacting the decadal increase in precipitation in the ITP. These results can improve our understanding of ITP summer precipitation attribution and can be applied to emergent constraints on future decadal precipitation prediction.

## INTRODUCTION

The water resource endowment in the Tibetan Plateau (TP) is critical to the supply of Asia's major rivers and feeds the downstream Asian population[1]. However, the rapid warming in recent decades has threatened the alpine water cycle and terrestrial water storage[2–7], which gives rise to the imbalance of the Asian water tower (referring to the TP)[8]. In particular, the changes in westerlies and Indian monsoon lead to the increased warm-season precipitation[8], resulting in increased runoff and accelerating accelerated lake expansion on the TP[9–13]. Hence, trends and multi-timescale variations in TP summer (June, July, and August) precipitation are vital to the terrestrial hydrological cycle and water resource management throughout many parts of Asia.

Evidence indicates that climate regime shift is the primary mechanism shaping the spatial-temporal variation of moisture transport and precipitation over the TP[14–18]. The discrepancies in dominant climate regimes and terrain result in substantial but spatially heterogeneous changes in precipitation, a drastic increase in the northern TP, and a statistical decrease in the exorheic basins of the southern TP[8,18,19]. Correspondingly, the lakes' number/area in the Inner TP (ITP) show the same decadal characteristics as that of summer precipitation[5,18]. Some progress has been made in understanding the physical mechanism of decadal variations in precipitation on the ITP[9,15,18]. The basin sea surface temperature (SST) anomalies (SSTA) in the Pacific, Atlantic,

and Indian Oceans exert great impacts in modulating global and regional climate change through air-sea interaction and tele-connection[20–25], which also contribute to the moisture transport and precipitation anomalies over the TP[15,18,26,27]. However, a comprehensive attribution of ITP precipitation changes in recent decades to external forcing and internal climate variability remains poorly understood.

The spatial-temporal precipitation variations over the TP are regulated by a combination of external forcing and internal climate variability[17,18,28–30]. This raised the question of what contributes to decadal variations in ITP summer precipitation. Here, we used a hierarchy of Community Earth System Model 1 simulation, including the large ensemble experiments (CESM-LE) and pacemaker runs, to identify the relative contribution and synergistic effects of external forcing and internally-driven variability on the decadal variations in ITP summer precipitation (see methods). The results provide a new insight to understand the causality of TP precipitation changes in the past and can also provide help to studies on constraining the future TP precipitation by the combination of external forcing and internal variability.

## RESULTS

### Emergence of increased ITP precipitation and lake expansion

Evidence of distinct decadal characteristics emerges from the temporal evolution of net moisture budget ($Q_T$) on the ITP derived

[1]Department of Atmospheric Science, School of Environmental Studies, China University of Geosciences, Wuhan, China. [2]Centre for Severe Weather and Climate and Hydrogeological hazards, Wuhan, China. [3]Nansen-Zhu International Research Centre, Institute of Atmospheric Physics, Chinese Academy of Sciences, Beijing, China. [4]Collaborative Innovation Center on Forecast and Evaluation of Meteorological Disasters/Key Laboratory of Meteorological Disaster, Ministry of Education, Nanjing University of Information Science and Technology, Nanjing, China. [5]Key Laboratory of Hydrometeorological Disaster Mechanism and Warning of Ministry of Water Resources/Collaborative Innovation Center on Forecast and Evaluation of Meteorological Disasters, Nanjing University of Information Science and Technology, Nanjing, China. ✉email: liuyong78@cug.edu.cn; hjwang@nuist.edu.cn
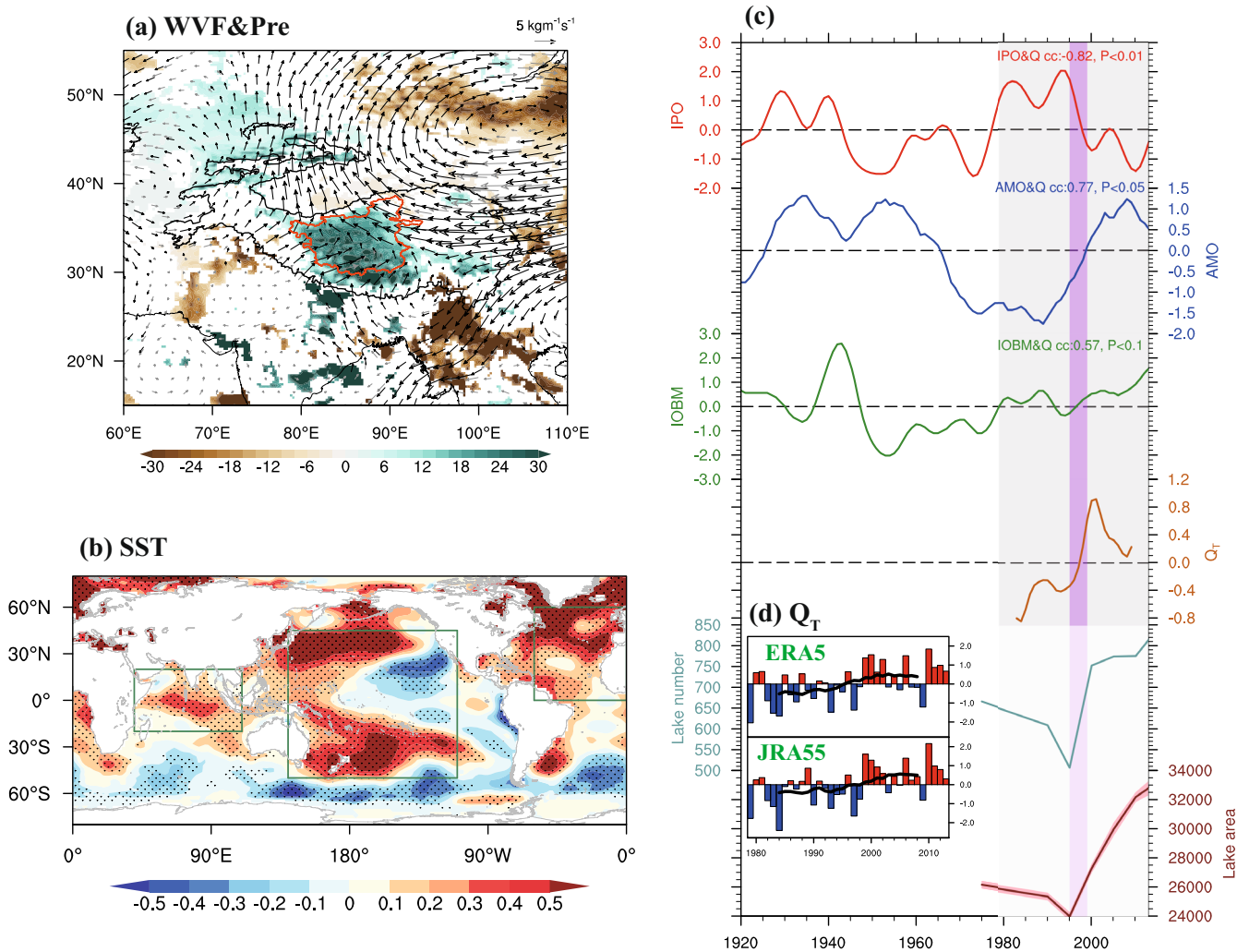
**Fig. 1 The interdecadal characteristics of summer precipitation on the ITP. a** The regression patterns of vertically integrated moisture flux (WVF; integrated from surface to 100 hPa; vector; $kgm^{-1}s^{-1}$) and summer precipitation (shading; mm/month) with regard to the $Q_T$ index. The shading and black vectors indicate that anomalies are significant at a confidence level of 95%. **b** The regression patterns of SST with regard to the $Q_T$ index. The dots indicate that anomalies are significant at a confidence level of 95%. **c** Time series of IPO (red line), AMO (blue line), IOBM (forest-green line), $Q_T$ (dark-orange line), lake numbers (cade-blue line), and total area of lakes (brown line) in the ITP. The light-pink shadow overlaid on the lake area curve represents the error. **d** Time series of the net moisture budget ($Q_T$) over the ITP (30°–36°N, 81°–91°E). The thick black line indicates the nine-year running average. All variables used for regression and correlation analyses were conducted by Lanczos nine-year low-pass filtering.

from ERA5 and JRA55 (Fig. 1d and Supplementary Fig. 1). The remarkable decadal transition corresponds well with the phase shift of the Interdecadal Pacific Oscillation (IPO), Atlantic Multi-decadal Oscillation (AMO) and Indian Ocean Basin Mode (IOBM) during 1979–2013. The dominant pattern of SST in the Pacific, Atlantic, and Indian Oceans show an intimate correlation with $Q_T$ at the decadal time scale, and the correlation coefficients are 0.82, 0.77, and 0.57 at 0.01, 0.05, and 0.1 significance level, respectively (Fig. 1b, c). Simultaneously, there were substantial changes in summer precipitation on the TP which are robust in station-observed records and all four gridded precipitation products (CMFD, APHRODITE, GPCC, and CRU) in this epoch (Fig. 1a and Supplementary Fig. 2). These changes involve significant increasing precipitation accompanied by moisture convergence over the ITP in the late 1990s (Fig. 1a). Consequently, the abundant precipitation prompts abrupt lake expansion over the ITP, with lakes' number growing from ~500 in the mid-1990s to more than 800 in 2013, directly causing the total area of lakes to increase by 35% to ~32,880 km² in 2013[9,31] (Fig. 1c).

**Decadal attribution of increased ITP summer precipitation**

Despite the changes in $Q_T$ statistically correlating with the basin SST variation, it is still hard to separate their roles in ITP precipitation changes. To address this question the observation and four sets of CESM ensemble simulations are employed to clarify the effects of external forcing and internally-driven variability on decadal variations in ITP precipitation. The selected period has been divided into two epochs P1 (1979–1998) and P2 (1999–2013) based on the results of regime shift detection (Supplementary Fig. 1; see methods). The decadal difference of SST between P1 and P2 for summer in observations and simulations are shown in Fig. 2. To distinguish the impacts of external forcing from the internal variability in the Pacific, Atlantic, and Indian Oceans, the CESM-LE ensemble mean is subtracted from the CESM pacemaker ensemble experiments (Fig. 2f–h). The methodology used in this study is demonstrated to reasonably separate the signals and reproduce the observations to a large extent[32]. Moreover, the synergistic effects of external forcing and internally-driven variability are also presented in this study (Fig. 2b–d). The observed SST anomalies identify an IPO-like mode in
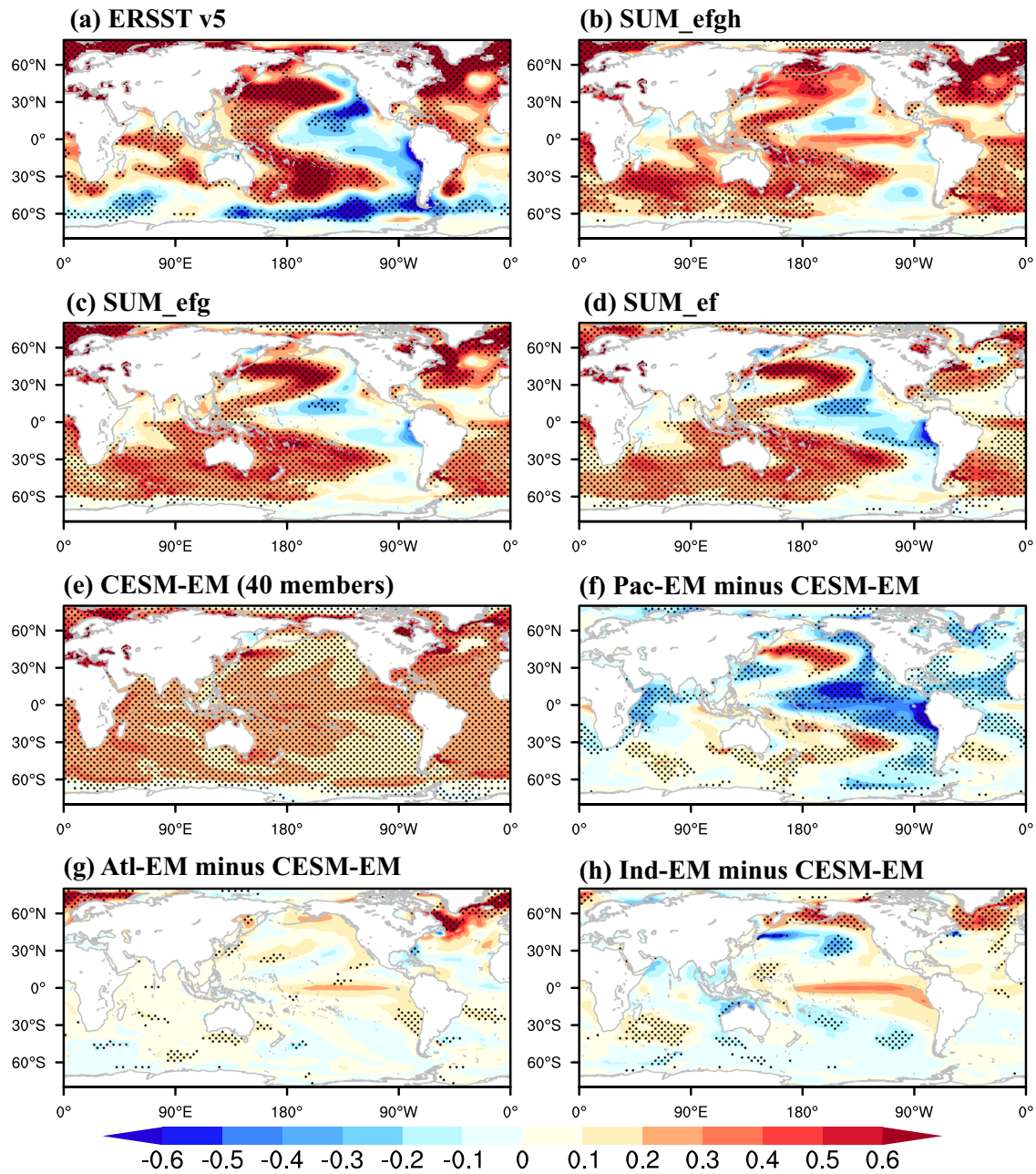
**Fig. 2** **The composite SST (K) pattern between P2 (1999–2013) and P1 (1979–1998). a** ERSST v5. **b** Sum of (**e**)–(**h**). **c** sum of (**e**)–(**g**). **d** Sum of (**e**, **f**). **e** CESM-LE ensemble mean (CESM-EM), indicative of external forcing. **f** Pacific pacemaker ensemble mean (Pac-EM) minus CESM-EM, indicative of internal variability due to the Pacific SST changes. **g** Atlantic pacemaker ensemble mean (Atl-EM) minus CESM-EM, indicative of internal variability due to the Atlantic SST changes. **h** Indian pacemaker ensemble mean (Ind-EM) minus CESM-EM, indicative of internal variability due to the Indian Ocean SST changes. The dots indicate that anomalies are significant at a confidence level of 95%.

the Pacific, an AMO-like mode in the Atlantic, and an IOBM-like mode in the Indian Ocean. This pattern can be reasonably reproduced by involving the component of external forcing and Pacific internal variability (Fig. 2d). This means the important role of anthropogenic forcing and internal decadal variability in the Pacific SST should be highlighted. However, the tropical Atlantic and Indian Ocean cannot reproduce the observed SST pattern (Fig. 2g, h).

Figure 3 shows the decadal differences in moisture flux and precipitation in response to individual basin internally-driven variability and a combination of external forcing and basin SST changes. The atmospheric circulation induced by Atlantic or Indian internal variability does not give rise to significant

precipitation changes on the ITP (Fig. 3g, h). The external forcing-induced cyclonic circulation over the western TP brings more moisture to the ITP and generates precipitation through enhancing westerlies (Fig. 3e and Supplementary Fig. 3e), while the weakened East Asian westerly jet (EAWJ) traps moisture on the ITP and increases precipitation when considering Pacific internal SST changes (Fig. 3f and Supplementary Fig. 4f). The sum of external and internal factors can roughly capture the atmospheric circulation characteristics observed in the reanalysis despite an eastward Baikal anticyclone, with the identified Rossby wave train over the middle and high latitudes and the weakened EAWJ (Supplementary Fig. 3a–d and Fig. 4a–d). Correspondingly, the simulations yield a similar pattern of precipitation to the
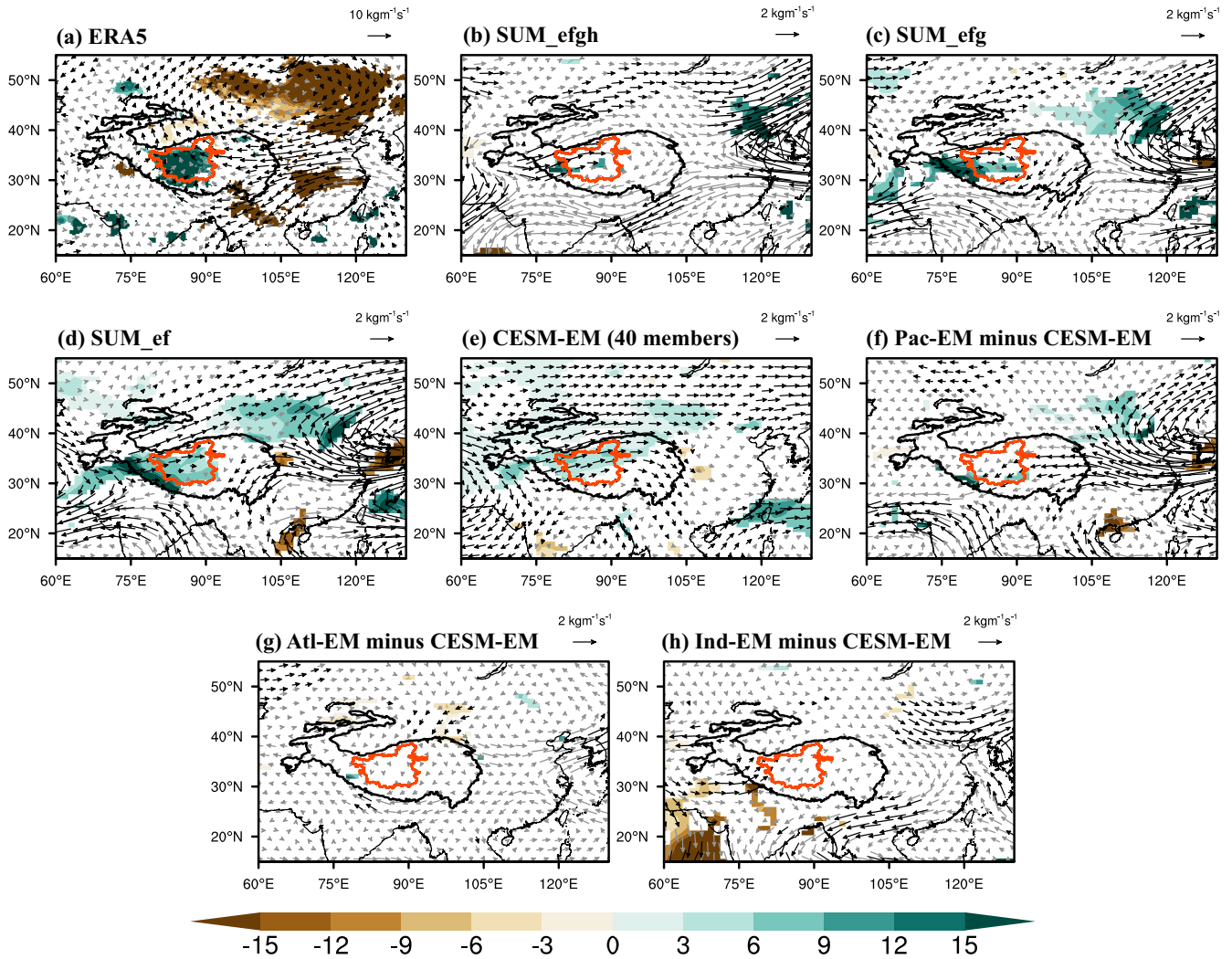
**Fig. 3  The composite integrated moisture flux (600–100 hPa; vectors; kgm$^{-1}$s$^{-1}$) and precipitation pattern (shading; mm/month) between P2 and P1. a** ERA5. **b** Sum of (**e**)–(**h**). **c** Sum of (**e**)–(**g**). **d** Sum of (**e**, **f**). **e** CESM-LE ensemble mean (CESM-EM). **f** Pacific pacemaker ensemble mean (Pac-EM) minus CESM-EM. **g** Atlantic pacemaker ensemble mean (Atl-EM) minus CESM-EM. **h** Indian Ocean pacemaker ensemble mean (Ind-EM) minus CESM-EM. The shading and black vectors indicate that anomalies are significant at a confidence level of 90%.

observations over the ITP (Fig. 3a–d), while the magnitude of precipitation decreases with additional superimposed impacts from Indian Ocean SST changes (Fig. 3b).

To quantify the attribution of decadal precipitation changes, the moisture budget analysis has been performed over the ITP. Observed results indicate that precipitation changes are mainly attributed to vertical moisture advection. Specifically, the thermo-dynamic component has preferred impacts on decadal changes in precipitation over the dynamic component (Fig. 4a). The strong uplift induced by dynamic convergence over the ITP is critical to the generation of summer precipitation (Supplementary Fig. 5a). Despite a credible precipitation increment occurring in the models, all simulations underestimate the climatological specific humidity and its variations (Supplementary Fig. 6, 7), resulting in a relatively small change of decomposed moisture budget terms involving the specific humidity (Fig. 4b, c). The external forcing contributes positively to the observed precipitation changes, while the dynamic component increases by about 2 times after considering the impacts of Pacific internal variability (Fig. 4c and Supplementary Fig. 5). Both of them can cumulatively account for ~41% of the observed precipitation changes. However, it does not cause additional notable changes when introducing the impacts of Atlantic and Indian Ocean intrinsic SST changes.

To investigate the atmospheric circulation changes in response to external forcing and Pacific internal variability, the generation and propagation of stationary Rossby wave were diagnosed (see methods). Observations indicate the atmospheric circulation anomalies related to the IPO are characterized by a distinct zonal wave train propagation (Fig. 5a). The Rossby wave sink on the Baikal and North Pacific caused by the vortex stretching contributes to the generation and maintenance of anticyclones (Supplementary Fig. 8, 9a), which further play an important role in decelerating the background EAWJ through easterlies on the south of anticyclones (Supplementary Fig. 10). Consequently, the strengthened westerlies induced by the anomalous cyclone and weakened westerlies over the eastern ITP are crucial to the moisture convergence and precipitation generation. The simulated results can capture the atmospheric dynamic feedback similar to the observations. Evidence suggests that the external forcing is responsible for the enhanced wave propagation over Eurasia and results in an anomalous cyclone on the western TP (Fig. 5b). While the Pacific pacemaker large ensemble simulations suggest that during the negative phase of the IPO, the convergence (divergence) over the Northwest Pacific (Northeast Asia and the seas to its east) gives rise to the generation of the Rossby wave source (RWS) or Rossby wave sink through vortex
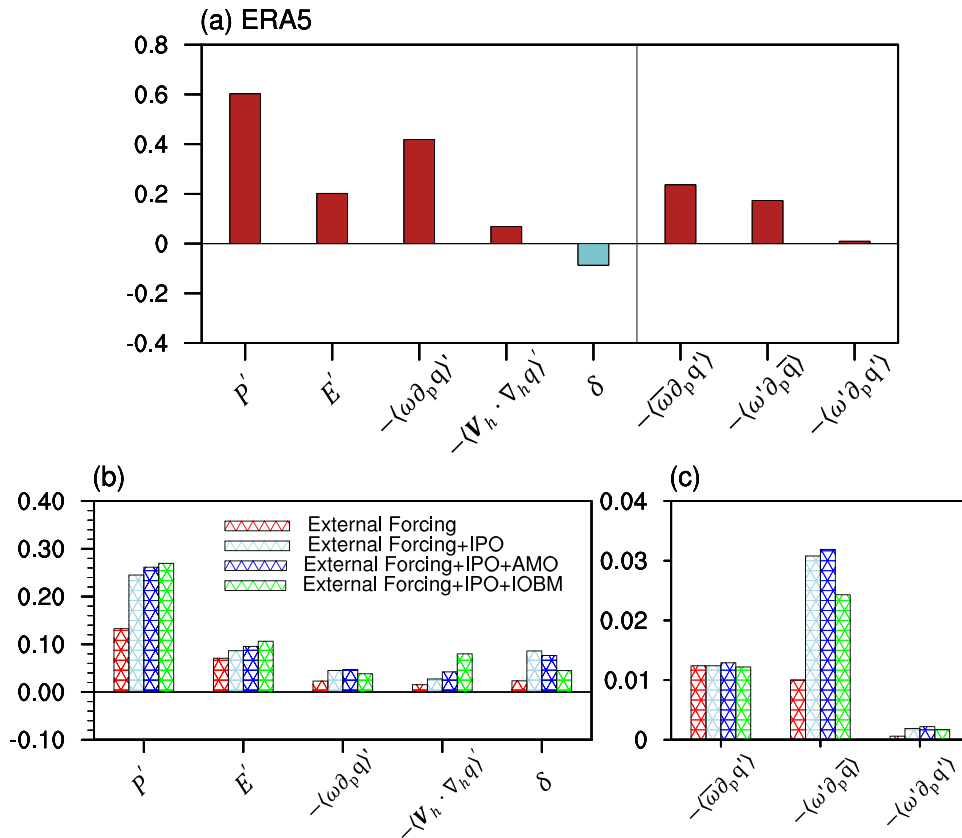
**Fig. 4 The decadal difference of moisture budget components averaged over the ITP between P2 and P1. a** ERA5. **b, c** CESM-EM (indicative of external forcing; red rectangle), external forcing plus Pacific internal SST changes (light-blue rectangle), external forcing plus Pacific and Atlantic internal SST changes (blue rectangle), and external forcing plus Pacific, Atlantic and Indian Ocean internal SST changes (green rectangle). $P'$ (mm/day) and $E'$ (mm/day) indicate the decadal difference of precipitation and evaporation, respectively. $-\langle V_h \cdot \nabla_h q \rangle'$, $-\langle \omega \partial_p q \rangle'$ and $\delta$ represent the changes in horizontal and vertical moisture advection, as well as the residual term, respectively. $-\langle \overline{\omega} \partial_p q' \rangle$ indicates the thermodynamic effects (the contribution of moisture change), $-\langle \omega' \partial_p \overline{q} \rangle$ indicates the dynamic effects (the contribution of atmospheric circulation change), and $-\langle \omega' \partial_p q' \rangle$ indicates the nonlinear component.

stretching, stimulating the meridional wave propagation and resulting in the anomalous dipole quasi-geostrophic stream function pattern on the North Pacific (Fig. 5c and Supplementary Fig. 8, 9b). Simultaneously, the advection of upper-level absolute vorticity by the southerly and westerly divergent flow on the North Pacific are nontrivial for changes in the RWS. Hence, the easterlies induced by the dipole pattern led to the deceleration of EAWJ.

The interaction between the mean flow and synoptic baroclinic eddies caused by the baroclinic instability has been reported to exert great impacts on westerly jet variations[24,33]. To further investigate the role of transient eddies in EAWJ, the transient eddy kinetic energy (TEKE) and E vector were applied (see methods). Both observations and simulations suggest the negative TEKE dominating East Asia was consistent with the convergence of the E vector, indicating the weakened transient eddy activities in response to a combination of external forcing and Pacific internal SST changes (Fig. 6). The reduced energy transformation from synoptic transient eddies to mean flow led to the weakened EAWJ.

**CMIP6 validation**

To illustrate whether this result is model-dependent, we use the pacemaker experiments from the Decadal Climate Prediction Project (DCPP) and Global Monsoons Model Intercomparison Project (GMMIP). Multi-member ensemble mean in different models can roughly reproduce the atmospheric circulation anomalies resembling CESM when involving the synergistic effects

of external forcing and Pacific internal variability, but the focus varies slightly between models (Supplementary Figs. 11–24). Results from IPSL-CM6A-LR large ensemble simulation indicate the external forcing exerts great impacts on the decadal enhancement of wave train propagation over Eurasia, and the weakened EAWJ could be attributed to the combination of external forcing and Pacific internal variability (Supplementary Figs. 12–14), which is also found in FGOALS-f3-L ensemble simulation (Supplementary Fig. 21). While the MRI-ESM2-0 ensemble mean yields a similar pattern with the observed atmospheric circulation for the decadal increased precipitation in the ITP (Supplementary Fig. 17–19). Additionally, all three CMIP6 models have better performance in simulating the summer specific humidity in the TP than CESM1.1, which can roughly capture the observed climatological mean precipitable water (figure not shown). Especially, among these CMIP6 models, MRI-ESM2-0 can basically reproduce the physical process of the decadal increased precipitation in the ITP, which highlights the synergistic effects of the thermodynamic effects and dynamic effects resembling the observations (Supplementary Fig. 20).

**DISCUSSION**

Over the past decades, the warming and wetting TP have shaped the water resource distribution pattern and resulted in the imbalance of the Asian water tower[8]. The decadal increase of precipitation accelerates lake expansion and keeps the glaciers in
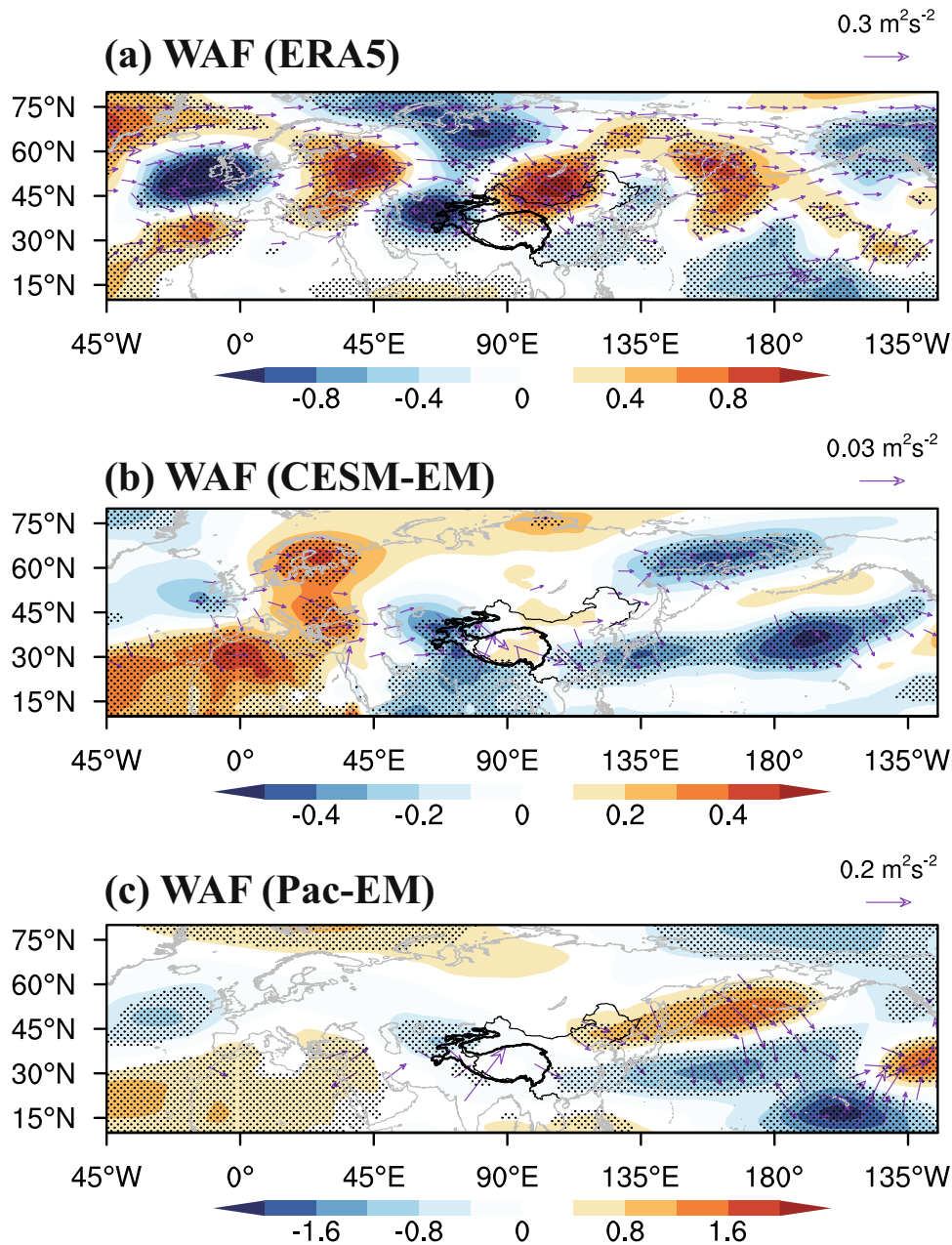
## (a) WAF (ERA5)

0.3 m²s⁻²



## (b) WAF (CESM-EM)

0.03 m²s⁻²



## (c) WAF (Pac-EM)

0.2 m²s⁻²



**Fig. 5 Observed and simulated stationary wave propagation in summer. a** The regression patterns of quasi-geostrophic stream (shading; 10⁶ m² s⁻¹) function and wave activity flux (vectors; m² s⁻²) at 200 hPa with regard to the IPO index (multiplied by −1). The decadal changes in quasi-geostrophic stream (shading; 10⁶ m² s⁻¹) function and wave activity flux (vectors m² s⁻²) between the P2 and P1 in (**b**) CESM-LE and (**c**) Pac-EM. The dots indicate that anomalies are significant at a confidence level of 95%.

the region dominated by the westerlies from shrinking under warming[34–36]. Concerns are growing over the decadal increase of summer precipitation and lakes' number/area over the ITP[2,5,18,37]. Despite some efforts having been made, the attribution of the decadal increase in ITP precipitation remains unclear.

Our results have demonstrated a robust decadal increase in summer precipitation on the ITP from 1979 to 2013. Both observations and large-ensemble simulations provide compelling evidence that the external forcing and Pacific internal variability are the dominant drivers of this increase, while the Atlantic and Indian internal variability has little impact on the decadal increase of ITP precipitation in the simulations. Notably, the increased precipitation prompts the abrupt lake expansion on the ITP, which reflects that climate warming significantly impacts the water resource redistribution in Asian water towers. We have also shown

that decadal changes in ITP precipitation are mainly attributed to the combination of thermodynamic and dynamic effects. Especially, the role of dynamic convergence over the ITP is significantly enhanced when involving the Pacific internal SST changes. Our evidence supports that the external forcing and internal variability induced by Pacific SSTs collaboratively result in the anomalous cyclone over the ITP and weakened EAWJ, which benefits the moisture convergence and precipitation generation over the ITP.

Our findings provide an in-depth understanding of decadal changes in ITP precipitation in response to climate warming on the decadal timescale. However, the underestimated specific humidity in the CESM1.1 hinders further study in revealing the thermodynamic mechanisms of precipitation changes. Evidence has also indicated that the CESM-LE simulations could ignore the role of specific humidity changes in precipitation generation,
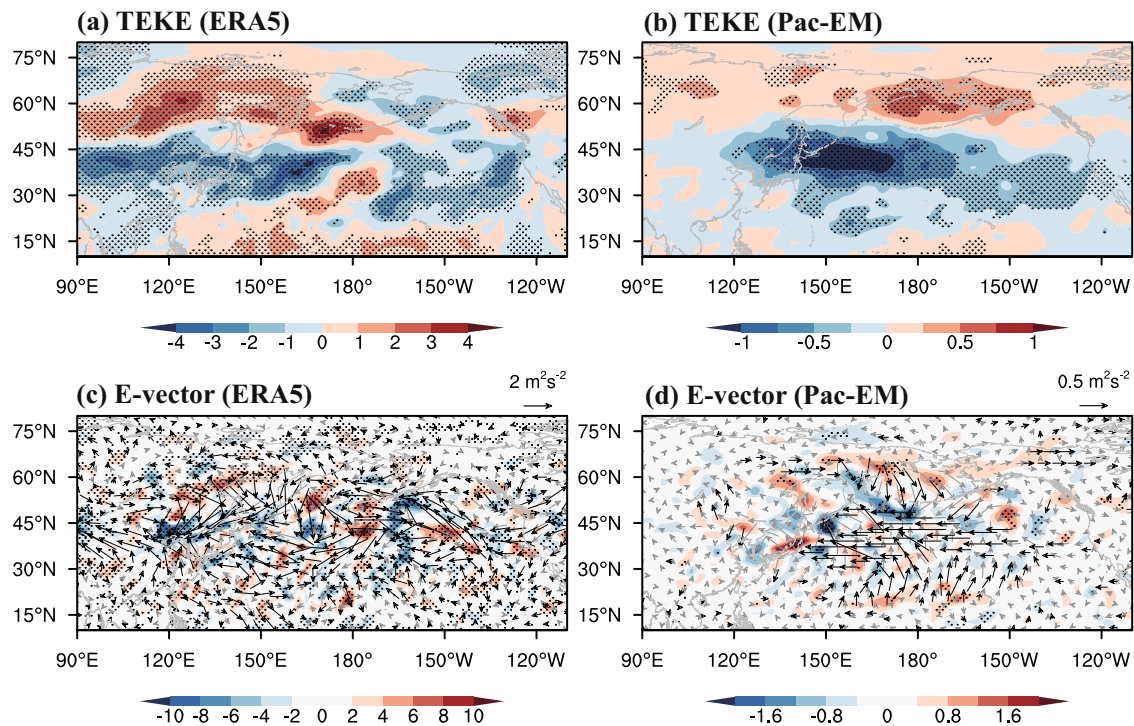
**Fig. 6 Observed and simulated transient dynamic process in summer.** The regression patterns of (**a**) transient eddy kinetic energy (TEKE; $m^2\ s^2$) and (**c**) E vector (vectors; $m^2\ s^{-2}$) and its divergence (shading; $10^{-6}\ m^2\ s^2$) at 200 hPa with regard to the IPO index (multiplied by $-1$). The decadal changes in (**b**) transient eddy kinetic energy (TEKE; $m^2\ s^2$) and (**d**) E vector (vectors; $m^2\ s^{-2}$) and its divergence (shading; $10^{-6}\ m^2\ s^2$) at 200 hPa. The dots indicate that anomalies are significant at a confidence level of 95%.

which led to a large divergence in physical attribution between simulations and observations. Furthermore, previous studies have highlighted the important role of AMO in modulating TP climate, while the Atlantic internal variability in the simulations does not cause significant changes in summer precipitation. It should be noted that the CESM-LE ensemble mean significantly suppressed the IPO variability, but gave rise to slightly strong AMO variability (Supplementary Fig. 25). The unremoved AMO variability may offset some impacts of Atlantic SST changes, resulting in the obscure change in ITP summer precipitation. Moreover, the complex topography of the TP may also be a reason that constrains the models from fully reproducing the physical process of the decadal increase in precipitation.

## METHODS

### Observational datasets

The daily in-situ precipitation from 88 meteorological stations around the TP from 1979 to 2013 is provided by the National Meteorological Information Center, China Meteorological Administration (CMA). The daily and monthly reanalysis dataset used in this study is ERA5[38], including geopotential height, horizontal winds, pressure velocity, specific humidity, and precipitation. The Japanese 55-year reanalysis (JRA-55)[39] is also used in this study, which demonstrated that it has good applicability in East Asia[40]. Moreover, multiple precipitation datasets are employed to verify the robustness of results due to the scarcity of meteorological stations on the central-western TP. The monthly precipitation data from the China Meteorological Forced Dataset (CMFD) is provided by He et al.[41]. Three gridded precipitation datasets are provided by the Asian Precipitation-Highly Resolved Observational Data Integration Toward the Evaluation (APHRODITE) of Water Resources project[42], the Global Precipitation Climatology Project (GPCP)[43], and the Climatic Research Unit gridded Time Series (CRU TS) dataset[44]. The monthly sea surface temperature

(SST) dataset is acquired from the National Oceanic and Atmosphere Administration Extended Reconstructed SST V5 dataset[45]. The lakes' number and area data in the Inner TP (ITP) are derived from Zhang et al.[31].

### CESM1 model design

To separate the influence of decadal variation in basin SST and the external forcing, four sets of Community Earth System Model version 1.1 (CESM1.1) experiments are used in this study. The first experiment is the CESM Large Ensemble (CESM-LE) with 40 individual members[46]. In addition to a slight difference in initial atmospheric temperature fields, all CESM-LE ensemble members adopt the same radiative forcing scenario, with historical forcing during 1920–2005 and the high-emission forcing scenario of representative concentration pathway 8.5 (RCP8.5) from 2006 to 2100. The individual CESM-LE ensemble member forced by small initial perturbations can reflect the internally generated variability of the climate system. When all CESM-LE ensemble members are averaged, the internal variability of the climate system is removed, and it represents the effects of external forcing[24]. The second is the CESM tropical Pacific Ocean pacemaker experiment, with fully restored observational SST anomalies (SSTA) applied over the region 15°S–15°N, 180° to the American coast, and two buffer belts along 15°–20°S and 15°–20°N. The buffer belts are identified as a transition region between the observational SST restored area and SSTA evolved freely area. In these buffer belts, the fully nudged SSTA are gradually damped to zero from the observational SST restored area to SSTA evolved freely area via a sine function of the latitude change. The third is the CESM tropical and North Atlantic SST, with fully restored observational SST anomalies (SSTA) applied over the region 5°–55°N, and two buffer belts for 0°–5°N and 55°–60°N. The last is the CESM tropical Indian Ocean pacemaker experiment, with fully restored observational SST anomalies (SSTA) applied over the region 15°S–15°N, and two buffer belts for 15°–20°S and 15°–20°N from the African coast to

180°. All pacemaker experiments are identical to the external forcing used in the CESM-LE with 10 ensemble members. Previous studies have indicated the ensemble mean of the ocean pacemaker experiment combines the response to external forcing and the response to observed time-varying SST changes in the SST restored area and buffer belts[24,47,48]. When subtracting the CESM-LE ensemble mean from the individual ocean pacemaker ensemble mean, we can obtain the climate response to the internal variability originating from the observed time-varying internally driven SST changes in the Pacific, Atlantic, and Indian Oceans, respectively. In this study, the methodology has been adopted to isolate the impacts of tropical Pacific, tropical and North Atlantic, and tropical Indian Ocean SST changes on the Tibetan Plateau (TP) summer precipitation. Moreover, to compare the synergistic effects of the external forcing and multiple Ocean internally driven SST changes and individual effects of tropical Pacific SST changes, we have designed two sets of experiments, one is the sum of four components (CESM-LE, plus the three pacemakers with external forcing removed), another one is the sum of three components (CESM-LE, plus the Pacific and Atlantic pacemakers with external forcing removed). But it is worth noting that this linear summation (the sum of external forcing and SST components) does not take into account tropical basin interactions and may result in excessive influence of tropical SSTs on the extratropical circulation[32].

### CMIP6 models
To validate the robustness of results derived from CESM1 experiments, we also analyzed the results of the Coupled Model Intercomparison Project Phase 6 (CMIP6) historical simulation, Decadal Climate Prediction Project (DCPP) pacemaker experiments, and Global Monsoons Model Intercomparison Project (GMMIP) pacemaker experiments[49]. Currently, only IPSL-CMA-LR provides both the Pacific pacemaker ensemble experiments (10 members) and Atlantic pacemaker ensemble experiments (10 members) in the DCPP, and the relevant control is the historical simulation (33 members). While in the GMMIP, only MRI-ESM2-0 provides both the Pacific and Atlantic Pacemaker experiments (3 members), and the historical simulation includes 10 members[50]. Moreover, we also used the historical simulation with 3 members and Pacific Pacemaker experiments with 3 members provided by FGOALS-f3-L. All these data are interpolated to a common grid of 1.0° × 1.0° using the bilinear interpolation method.

### Moisture budget analysis
The vertically integrated water vapor flux ($Q$) and net moisture budget ($Q_T$) are defined by Eqs. (1) and (2), respectively, as

$$Q = -\frac{1}{g}\int_{P_s}^{P} q\boldsymbol{V}\,dp \tag{1}$$

$$Q_T = \oint Q\,dl \tag{2}$$

where $g$, $p$, $ps$, $q$, $\boldsymbol{V}$, $l$ is the acceleration of gravity, pressure, surface pressure, specific humidity, horizontal wind, and the length of the boundary, respectively. The net moisture budget is obtained by calculating the sum of net inputs of water vapor fluxes at the four boundaries of Inner TP (30°–36°N, 81°–91°E).

The precipitable water ($W$) is also employed to evaluate the models' performance in simulating the specific humidity:

$$W = \frac{1}{g}\int_{P_s}^{p} q\,dp \tag{3}$$

The moisture budget analysis is used to investigate the physical mechanism of TP summer precipitation changes[51]. The vertically

integrated moisture budget equation is expressed as

$$P' = E' - \langle \boldsymbol{V}_h \cdot \nabla_h q\rangle' - \langle \omega\partial_p q\rangle' + \delta \tag{4}$$

where $P$, $E$, $q$, $\boldsymbol{V}_h$, and $\omega$ are precipitation, evaporation, specific humidity, horizontal wind, and vertical pressure velocity, respectively. ◇ means a vertical integration from the surface to 100 hPa. $-\langle \boldsymbol{V}_h \cdot \nabla_h q\rangle'$ and $-\langle \omega\partial_p q\rangle'$ represents the changes in horizontal and vertical moisture advection, respectively. $\delta$ indicates the residual term. The changes in $-\langle \omega\partial_p q\rangle'$ can be divided into the thermodynamic ($-\langle \overline{\omega}\partial_p q'\rangle$), dynamic effects ($-\langle \omega'\partial_p \overline{q}\rangle$), and nonlinear component ($-\langle \omega'\partial_p q'\rangle$):

$$-\langle \omega\partial_p q\rangle' = -\langle \overline{\omega}\partial_p q'\rangle - \langle \omega'\partial_p \overline{q}\rangle - \langle \omega'\partial_p q'\rangle \tag{5}$$

The thermodynamic term indicates the contribution of moisture change, while the dynamic term indicates the contribution of atmospheric circulation change.

### Eddy geopotential height
The eddy geopotential height anomalies are identified as the height anomalies from the zonal mean.

### Takaya–Nakamura (TN) wave activity flux and Rossby wave source (RWS)
The TN wave activity flux and RWS are introduced to diagnose the generation and propagation of stationary Rossby waves. The horizontal wave activity flux proposed by Takaya and Nakamura[52] is defined as

$$W = \frac{P}{2|\boldsymbol{U}|}\begin{pmatrix} \overline{u}\left(\psi_x'^2 - \psi'\psi_{xx}'\right) + \overline{v}\left(\psi_x'\psi_y' - \psi'\psi_{xy}'\right) \\ \overline{u}\left(\psi_x'\psi_y' - \psi'\psi_{xy}'\right) + \overline{v}\left(\psi_y'^2 - \psi'\psi_{yy}'\right) \end{pmatrix} \tag{6}$$

where $\boldsymbol{U}$ indicates the horizontal wind velocity, $\psi$ represents the stream function. The overbars and primes denote the climatology mean and seasonal disturbances, respectively.

The RWS is derived from the simplified barotropic vorticity equation[53,54]:

$$\frac{\partial \xi_a}{\partial t} + \boldsymbol{V}_\psi \cdot \nabla \xi_a = -\xi_a \nabla \cdot \boldsymbol{V}_\chi - \boldsymbol{V}_\chi \cdot \nabla \xi_a = -\nabla \cdot (\boldsymbol{V}_\chi \xi_a) \tag{7}$$

where $\xi_a$, $\boldsymbol{V}_\psi$, and $\boldsymbol{V}_\chi$ indicate the absolute vorticity, rotational winds, and divergent winds, respectively. The right term ($-\nabla \cdot (\boldsymbol{V}_\chi \xi_a)$) is defined as the RWS[55]. Especially, $-\xi_a \nabla \cdot \boldsymbol{V}_\chi$ denotes the vortex stretching, illustrating the changes in vorticity induced by upper-tropospheric convergence and divergence. $-\boldsymbol{V}_\chi \cdot \nabla \xi_a$ denotes the vortex advection, referring to the changes in vorticity related to the advection of absolute vorticity gradient by the divergent flow.

### Transient eddy kinetic energy (TEKE) and E vector diagnosis
The TEKE and E vector are introduced to diagnose the interactions between the mean flow and transient eddies. The TEKE and horizontal E vector are defined as follows:

$$TEKE = \frac{1}{2}(u'^2 + v'^2) \tag{8}$$

$$E = \left[\frac{1}{2}\left(\overline{v'^2} - \overline{u'^2}\right), -\overline{u'v'}\right] \tag{9}$$

where $u'$ and $v'$ indicate the synoptic components of the zonal and meridional winds. The transient variables are obtained by a 21-point Lanczos 2-8-day filtering and are on 200 hPa. The overbar represents the seasonal mean. The convergence and divergence of the E vector illustrate the feedback of transient eddies on the mean flow. When the E vector converges, the kinetic energy from synoptic eddies will be converted into time mean flow, which accelerates the westerly jet, and vice versa.

## Statistical methods

The moving *t-test* and Lepage method[56] are utilized to determine the decadal transition period. The Lanczos nine-year low-pass filtering is employed to preserve the decadal signal. To remove the effects of high autocorrelation induced by low-pass filtering, the effective number of degrees of freedom $N_{eff}$ is used[57]:

$$N_{eff} \approx \frac{N}{1 + 2\sum_{\tau=1}^{10} \frac{N-\tau}{N} r_X(\tau) r_Y(\tau)} \tag{10}$$

where $N$ is data length, and $r_X(\tau)$, $r_Y(\tau)$ is the autocorrelation of time series $X$, $Y$ with a lag of $\tau$ years.

## SST mode index

The Interdecadal Pacific Oscillation (IPO) and Atlantic Multi-decadal Oscillation (AMO) index data from 1920 to 2013 are derived as in Henley et al.[58] and Trenberth and Shea[59]. The IPO index is defined as the difference between the SSTA averaged over the central equatorial Pacific (10°S–10°N, 170°E–90°W) and the average of the SSTA in the Northwest (25°–45°N, 140°E–145°W) and Southwest Pacific (15°–50°S, 150°E–160°W). The AMO index is calculated as the average SSTA in the North Atlantic basin (0–60°N, 80°W–0°W). The Indian Ocean Basin Mode (IOBM) is obtained from the SSTA averaged over the tropical Indian Ocean (20°S–20°N, 40°–110°E).

## DATA AVAILABILITY

The CMA stational observed data can be available at http://data.cma.cn/. The CMFD precipitation data can be available at https://data.tpdc.ac.cn/zh-hans/data/8028b944-daaa-4511-8769-965612652c49/. The CRU TS precipitation dataset can be available at https://crudata.uea.ac.uk/cru/data/hrg/cru_ts_4.05/cruts.2103051243.v4.05/pre/. The APH-RODITE precipitation dataset can be available at https://www.chikyu.ac.jp/precip/english/. The GPCP precipitation dataset can be available at https://climatedataguide.ucar.edu/climate-data/gpcp-monthly-global-precipitation-climatology-project. The ERA5 reanalysis dataset can be downloaded at https://www.ecmwf.int/en/forecasts/datasets/reanalysis-datasets/era5. The JRA55 reanalysis dataset can be downloaded at https://jra.kishou.go.jp/JRA-55/index_en.html. The ERSST v5 data can be available at https://psl.noaa.gov/data/gridded/data.noaa.ersst.v5.html. The CESM1.1 dataset can be available at https://www.earthsystemgrid.org/. The CMIP5 data can be available at https://esgf-node.llnl.gov/projects/cmip6/. The IPO index is available at https://psl.noaa.gov/data/timeseries/IPOTPI/. The AMO index is available at https://climatedataguide.ucar.edu/climate-data/atlantic-multi-decadal-oscillation-amo. The IOBM index can be calculated from the ERSST v5 data. The lakes data in the ITP can be available at https://agupubs.onlinelibrary.wiley.com/doi/full/10.1002/2016GL072033.

## CODE AVAILABILITY

The data in this study were processed and plotted by the Climate Data Operators (CDO) and NCAR Command Language (NCL). Codes used in this study are available upon request.

## REFERENCES

1. Li, X. et al. Climate change threatens terrestrial water storage over the Tibetan Plateau. *Nat. Clim. Change* **12**, 801–807 (2022).
2. Yao, T. et al. Recent Third Pole's rapid warming accompanies cryospheric melt and water cycle intensification and interactions between monsoon and environment: multidisciplinary approach with observations, modeling, and analysis. *Bull. Am. Meteorol. Soc.* **100**, 423–444 (2019).
3. Immerzeel, W. W., van Beek, L. P. & Bierkens, M. F. Climate change will affect the Asian water towers. *Science* **328**, 1382–1385 (2010).
4. Yao, T. et al. Different glacier status with atmospheric circulations in Tibetan Plateau and surroundings. *Nat. Clim. Change* **2**, 663–667 (2012).
5. Zhang, G. et al. Response of Tibetan Plateau lakes to climate change: Trends, patterns, and mechanisms. *Earth-Sci. Rev.* **208**, 103269 (2020).
6. Kraaijenbrink, P., Stigter, E., Yao, T. & Immerzeel, W. W. Climate change decisive for Asia's snow meltwater supply. *Nat. Clim. Change* **11**, 1–7 (2021).
7. Jouberton, A. et al. Warming-induced monsoon precipitation phase change intensifies glacier mass loss in the southeastern Tibetan Plateau. *Proc. Natl Acad. Sci. USA* **119**, e2109796119 (2022).
8. Yao, T. et al. The imbalance of the Asian water tower. *Nat. Rev. Earth Environ.* **3**, 618–632 (2022).
9. Chen, W. et al. What Controls Lake Contraction and Then Expansion in Tibetan Plateau's Endorheic Basin Over the Past Half Century? *Geophys. Res. Lett.* **49**, e2022GL101200 (2022).
10. Lutz, A. F., Immerzeel, W. W., Shrestha, A. B. & Bierkens, M. F. P. Consistent increase in High Asia's runoff due to increasing glacier melt and precipitation. *Nat. Clim. Change* **4**, 587–592 (2014).
11. Yang, K. et al. Response of hydrological cycle to recent climate changes in the Tibetan Plateau. *Clim. Change* **109**, 517–534 (2011).
12. Lei, Y. et al. Response of inland lake dynamics over the Tibetan Plateau to climate change. *Clim. Change* **125**, 281–290 (2014).
13. Wu, Y. et al. Reconstructed eight-century streamflow in the Tibetan Plateau reveals contrasting regional variability and strong nonstationarity. *Nat. Commun.* **13**, 6416 (2022).
14. Dong, W. et al. Summer rainfall over the southwestern Tibetan Plateau controlled by deep convection over the Indian subcontinent. *Nat. Commun.* **7**, 10925 (2016).
15. Sun, J. et al. Why has the Inner Tibetan Plateau become wetter since the mid-1990s? *J. Clim.* **33**, 8507–8522 (2020).
16. Li, L., Zhang, R., Wen, M. & Lv, J. Regionally Different precipitation trends over the Tibetan Plateau in the warming context: a perspective of the Tibetan Plateau vortices. *Geophys. Res. Lett.* **48**, e2020GL091680 (2021).
17. Hu, S., Zhou, T. & Wu, B. Impact of developing ENSO on Tibetan Plateau summer rainfall. *J. Clim.* **34**, 3385–3400 (2021).
18. Liu, Y., Chen, H., Li, H., Zhang, G. & Wang, H. What induces the interdecadal shift of the dipole patterns of summer precipitation trends over the Tibetan Plateau? *Int. J. Climatol.* **41**, 5159–5177 (2021).
19. Kuang, X. & Jiao, J. J. Review on climate change on the Tibetan Plateau during the last half century. *J. Geophys. Res.: Atmos.* **121**, 3979–4007 (2016).
20. Sutton, R. T. & Hodson, D. L. Atlantic Ocean forcing of North American and European summer climate. *Science* **309**, 115–118 (2005).
21. Ueda, H. et al. Combined effects of recent Pacific cooling and Indian Ocean warming on the Asian monsoon. *Nat. Commun.* **6**, 8854 (2015).
22. Zhang, R. & Delworth, T. L. Impact of the Atlantic Multidecadal Oscillation on North Pacific climate variability. *Geophys. Res. Lett.* **34**, L23708 (2007).
23. Goswami, B. N., Madhusoodanan, M. S., Neema, C. P. & Sengupta, D. A physical mechanism for North Atlantic SST influence on the Indian summer monsoon. *Geophys. Res. Lett.* **33**, L02706 (2006).
24. Huang, D. et al. Contributions of different combinations of the IPO and AMO to recent changes in winter East Asian jets. *J. Clim.* **32**, 1607–1626 (2019).
25. Zhang, J., Hu, R., Ma, Q. & Niu, M. The warming of the Arabian Sea induced a northward summer monsoon over the Tibetan Plateau. *J. Clim.* **35**, 3941–3954 (2022).
26. Zhou, C., Zhao, P. & Chen, J. The interdecadal change of summer water vapor over the Tibetan Plateau and associated mechanisms. *J. Clim.* **32**, 4103–4119 (2019).
27. Zhao, L., Simon Wang, S. Y. & Meyer, J. Interdecadal climate variations controlling the water level of lake Qinghai over the Tibetan Plateau. *J. Hydrometeorol.* **18**, 3013–3025 (2017).
28. Zhao, D., Zhang, L. & Zhou, T. Detectable anthropogenic forcing on the long-term changes of summer precipitation over the Tibetan Plateau. *Clim. Dyn.* **59**, 1939–1952 (2022).
29. Duan, W. et al. Evaluation and future projection of Chinese precipitation extremes using large ensemble high-resolution climate simulations. *J. Clim.* **32**, 2169–2183 (2019).
30. Duan, W. et al. Changes in temporal inequality of precipitation extremes over China due to anthropogenic forcings. *npj Clim. Atmos. Sci.* **5**, 33 (2022).
31. Zhang, G. et al. Extensive and drastically different alpine lake changes on Asia's high plateaus during the past four decades. *Geophys. Res. Lett.* **44**, 252–260 (2017).
32. Yang, D. et al. Role of tropical variability in driving decadal shifts in the Southern Hemisphere summertime eddy-driven jet. *J. Clim.* **33**, 5445–5463 (2020).
33. Wang, N., Jiang, D. & Lang, X. Seasonality in the response of East Asian westerly jet to the Mid-Holocene forcing. *J. Geophys. Res.: Atmos.* **125**, e2020JD033003 (2020).
34. Brun, F., Berthier, E., Wagnon, P., Kaab, A. & Treichler, D. A spatially resolved estimate of High Mountain Asia glacier mass balances, 2000–2016. *Nat. Geosci.* **10**, 668–673 (2017).
35. Dehecq, A. et al. Twenty-first century glacier slowdown driven by mass loss in High Mountain Asia. *Nat. Geosci.* **12**, 22–27 (2018).

36. Forsythe, N., Fowler, H. J., Li, X.-F., Blenkinsop, S. & Pritchard, D. Karakoram temperature and glacial melt driven by regional atmospheric circulation variability. *Nat. Clim. Change* **7**, 664–670 (2017).

37. Yang, K. et al. Recent climate changes over the Tibetan Plateau and their impacts on energy and water cycle: a review. *Glob. Planet. Change* **112**, 79–91 (2014).

38. Hersbach, H. et al. The ERA5 global reanalysis. *Q. J. R. Meteorological Soc.* **146**, 1999–2049 (2020).

39. Ebita, A. et al. The Japanese 55-year Reanalysis "JRA-55": An Interim Report. *Sola* **7**, 149–152 (2011).

40. Yang, S., Lau, K.-M. & Kim, K.-M. Variations of the East Asian jet stream and Asian–Pacific–American winter climate anomalies. *J. Clim.* **15**, 306–325 (2002).

41. He, J. et al. The first high-resolution meteorological forcing dataset for land process studies over China. *Sci. Data* **7**, 25 (2020).

42. Yatagai, A. et al. APHRODITE: constructing a long-term daily gridded precipitation dataset for Asia based on a dense network of rain gauges. *Bull. Am. Meteorol. Soc.* **93**, 1401–1415 (2012).

43. Huffman, G. J. et al. Global precipitation at one-degree daily resolution from multisatellite observations. *J. Clim.* **2**, 36–50 (2001).

44. Harris, I., Osborn, T. J., Jones, P. & Lister, D. Version 4 of the CRU TS monthly high-resolution gridded multivariate climate dataset. *Sci. Data* **7**, 109 (2020).

45. Huang, B. et al. Extended reconstructed sea surface temperature, version 5 (ERSSTv5): upgrades, validations, and intercomparisons. *J. Clim.* **30**, 8179–8205 (2017).

46. Kay, J. E. et al. The Community Earth System Model (CESM) Large Ensemble project: a community resource for studying climate change in the presence of internal climate variability. *Bull. Am. Meteorol. Soc.* **96**, 1333–1349 (2015).

47. Holland, P. R., Bracegirdle, T. J., Dutrieux, P., Jenkins, A. & Steig, E. J. West Antarctic ice loss influenced by internal climate variability and anthropogenic forcing. *Nat. Geosci.* **12**, 718–724 (2019).

48. Schneider, D. P. & Deser, C. Tropically driven and externally forced patterns of Antarctic sea ice change: reconciling observed and modeled trends. *Clim. Dyn.* **50**, 4599–4618 (2017).

49. Boer, G. J. et al. The Decadal Climate Prediction Project (DCPP) contribution to CMIP6. *Geoscientific Model Dev.* **9**, 3751–3777 (2016).

50. Zhou, T. et al. GMMIP (v1.0) contribution to CMIP6: Global Monsoons Model Inter-comparison Project. *Geoscientific Model Dev.* **9**, 3589–3604 (2016).

51. Seager, R., Naik, N. & Vecchi, G. A. Thermodynamic and dynamic mechanisms for large-scale changes in the hydrological cycle in response to global warming*. *J. Clim.* **23**, 4651–4668 (2010).

52. Takaya, K. & Nakamura, H. A formulation of a phase-independent wave-activity flux for stationary and migratory quasigeostrophic eddies on a zonally varying basic flow. *J. Atmos. Sci.* **58**, 608–627 (2001).

53. Hartman, D. L. The atmospheric general circulation and its variability. *J. Meteorol. Soc. Jpn.* **85B**, 123–143 (2007).

54. Shimizu, M. H. & de Albuquerque Cavalcanti, I. F. Variability patterns of Rossby wave source. *Clim. Dyn.* **37**, 441–454 (2010).

55. Sardeshmukh, P. D. & Hoskins, B. J. The generation of global rotational flow by steady idealized tropical divergence. *J. Atmos. Sci.* **45**, 1228–1251 (1998).

56. Lepage, Y. A combination of Wilcoxon's and Ansari-Bradley's statistics. *Biometrika* **58**, 213–217 (1971).

57. Pyper, B. J. & Peterman, R. M. Comparison of methods to account for auto-correlation in correlation analyses of fish data. *Can. J. Fish. Aquat. Sci.* **55**, 2127–2140 (1998).

58. Henley, B. J. et al. A Tripole Index for the Interdecadal Pacific Oscillation. *Clim. Dyn.* **45**, 3077–3090 (2015).

59. Trenberth, K. E. & Shea, D. J. Atlantic hurricanes and natural variability in 2005. *Geophys. Res. Lett.* **33**, L12704 (2006).

## AUTHOR CONTRIBUTIONS
Y.L. and H.W. developed the essential research idea and designed the experiments. Y.L. performed the analysis and wrote the manuscript. Others contributed to the interpretation of the results and the preparation of the manuscript.

## COMPETING INTERESTS
The authors declare no competing interests.

## ADDITIONAL INFORMATION
**Supplementary information** The online version contains supplementary material available at https://doi.org/10.1038/s41612-023-00369-4.

**Correspondence** and requests for materials should be addressed to Yong Liu or Huijun Wang.

**Reprints and permission information** is available at http://www.nature.com/reprints

**Publisher's note** Springer Nature remains neutral with regard to jurisdictional claims in published maps and institutional affiliations.